ISSN: 2634-9221
European Journal of Applied Sciences; Vol. 14 No. 05 (2026) (135-162)
https://doi.org/10.14738/ejas.1405.12204

Effect of Transition Metal Ions on the Physicochemical Properties of Glass Produced from Rice Husk Based Silica and Periwinkle Shells

Ogunkunle, Olaoluwa Ayobami[1], Adeojo, Oluwamumiyo Dorcas[2], Komolafe, Emmanuel Blessing[1], Agosile, Blessing Akorede[1], Adewale, Abdulafeez Olalekan[1] and Adebayo, Samuel Ayomide[1]

1. Department of Chemistry, Faculty of Science, Obafemi Awolowo University, Ile-Ife, Osun State, Nigeria
2. Department of Chemistry, Faculty of Science, University of Ibadan, Ibadan, Oyo State, Nigeria

Abstract: Agricultural residues and biogenic wastes from food production are often poorly managed, contributing significantly to environmental pollution. This research repurposed such wastes as raw inputs for producing valuable products, thereby reducing pollution harmful to humans, animals, and plants. Rice husks, noted for their high silica content, and calcium-rich periwinkle shells were utilized. EDXRF analysis revealed silica (10.32 %W) and calcium (31.05 %W) in the mineralized rice husks and periwinkle shells, along with phosphorus (0.62 %W and 0.25 %W, respectively). Silicate glass samples were synthesized using alkali-extracted silica from rice husks and periwinkle shells with a flux, while transition metal-doped glasses were produced by adding Fe^{3+}, Co^{2+}, Ni^{2+} and Cu^{2+} salts. FT-IR analysis confirmed Si–OH and Si–O–Si groups in silica, and Ca–O and P–O bands in the periwinkle shells, with evidence of chelation through Si–OH interactions and M–O bonding. UV-visible spectra showed d–d transitions that affected absorbance, transmittance, colouration, and geometric structures of the doped glasses. SEM analysis revealed crystalline and semi-crystalline microstructures in the flint glass, which became more crystalline with transition metals doping. All glasses produced were stable, with flint glass showing the highest mechanical strength. Among the doped samples, Fe^{3+}-doped glass exhibited the greatest stability, while Cu^{2+}-doped glass showed the lowest strength and stability.

Keywords: *Periwinkle shell, Rice Husk, Transition metal ions, Doped flint glass, Crystallinity.*

INTRODUCTION

Agricultural and marine wastes are abundant by-products that often lack sustainable disposal routes, thereby leading to pollution and ecosystem degradation. Rice husks, constituting about 20% of harvested rice, are silica-rich residues typically discarded by burning or landfill, releasing harmful particulates and gases. Similarly, periwinkle shells typically comprising 60–70% of the animal's weight, are largely composed of calcium carbonate and are often indiscriminately disposed in coastal areas. Their mismanagement results in odour, leaching of contaminants, and emission of toxic gases and other environmental challenges which are significant enough to cause health problems for humans, animals and ecosystem at large.

Glass production traditionally relies on high-purity silica sand, limestone, and soda ash. However, extracting these resources carries significant ecological and economic costs. Rice husk ash provides an abundant alternative source of amorphous silica, while periwinkle shells is a good source of calcium carbonate, both essential constituents in soda–lime glass. By valorizing these wastes, sustainable and cost-effective glass can be produced, reducing dependence on non-renewable raw materials. This research aimed at:

1. Extracting silica from mineralized rice husk ash and calcium oxide from periwinkle shells for glass production.
2. Producing soda–lime glass using these waste materials.
3. Studying the effects of Cu(II), Co(II), Fe(III) and Ni(III) ions on the physicochemical properties of the produced glass.

MATERIALS AND METHODS

Materials

The experimental samples for this study comprising of rice husks, periwinkle shells, iron rust, and some transition metal salts were available in a relatively high abundance. Three different batches of rice husks were collected for the purpose of this study based on the following parameters;

1. Method of dehusking.
2. Period of existence (storage).

The sampling methods were aimed at studying the effect of dehusking methods and storage on the quality and quantity of the silica obtained from the different rice husk samples. The first set of the rice husk samples (Fig. 1) were collected from a farmland in Marte located in Tafawa Balewa Local Government Area of Bauchi State in the Northern part of Nigeria. The choice was based on the mechanical method of dehusking that is the most prevalent in the area.

The second set of the rice husk samples (Fig. 2) collected in this study were collected from a farmland in Igbemo-Ekiti located in Irepodun/Ifelodun Local Government Area of Ekiti State, Nigeria. This set, unlike the other two sets of rice husks, was thermomechanically dehusked and collected after a short period of storage time.

The third set of the rice husk samples (Fig. 3) originated from a farmland located in Egbedore Local Government Area, Osun State and were collected from a store at the Department of Material Science and Engineering in Obafemi Awolowo University, Ile-Ife, Osun State, where it had been stored and preserved for about 3 years. Its choice complimented the second parameter for the collection of the rice husks samples. Periwinkle shells, which are another essential raw material in this study were also collected from the retailer at Ojuelegba Market in Surulere Local Government Area, of Lagos State where they were available in commercial quantity after the edible part of the animal mass had been extracted (Fig 4).

The transition metal salts used in this study which are copper sulphate, nickel chloride and cobalt chloride were of analytical grade obtained from a reputable chemical vendor.

Figure 1: Mechanically Dehusked Rice Husk Samples.

Figure 2: Thermomechanically Dehusked Rice Husk Samples.

Figure 3: Stored Rice Husk Samples (Stale).

Figure 4: Periwinkle Shells

Extraction of Silica from the Rice Husks

This stage consists of stepwise processes involved in the conversion of the raw rice husks obtained from different sources into naturally occurring silica required for the purpose of this study. It is essential to note that the silica obtained in this study is slightly different from the conventional silica because it is obtained from a biological source which is an agricultural residue.

Mineralization of the Rice Husks

The rice husk samples were subjected to mineralization through controlled thermal decomposition at 850 °C for four hours, a process that ensured the removal of organic matter while preserving the inherent mineral constituents (*Okonkwo et al., 2019; Kumar et al., 2021*). The procedure was repeated until sufficient quantity of ashes were obtained. The resulting mineralized products were subsequently stored in airtight containers to prevent contamination and maintain their integrity for further experimental applications (*AOAC, 2019; Yalcin et Sevinc, 2001*).

Heat Induced Alkaline Extraction of Silica from Rice Husk Ash

The extraction of silica from the mineralized rice husk ash was achieved through alkaline treatment using 1 M NaOH solution in excess, which was applied to a known mass of ash under controlled heating for one hour. This process facilitated the dissolution of silica, producing a dark-colored solution indicative of sodium silicate formation *(Kumar et al., 2021; Yalcin et Sevinc, 2001; Liou, 2004; Kalapathy et al., 2000*). After cooling, the mixture was filtered under suction to yield a clear golden filtrate identified as sodium silicate. Silica was subsequently precipitated by the gradual addition of 1 M HCl to the sodium silicate solution at a 2:1 ratio under heating, leading to the formation of gelatinous silica due to the abrupt pH change. The gel was filtered, compressed to remove residual water, and then oven-dried at 150 °C for 10 hours to obtain crystalline silica. The final product was stored in airtight containers to prevent moisture uptake and contamination.

$$SiO_{2(s)} + 2NaOH_{(l)} \rightarrow Na_2SiO_{3(l)} + H_2O_{(l)}$$

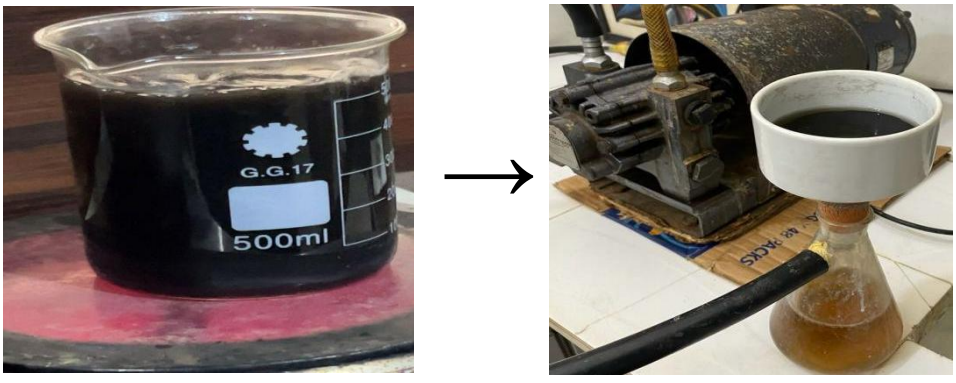

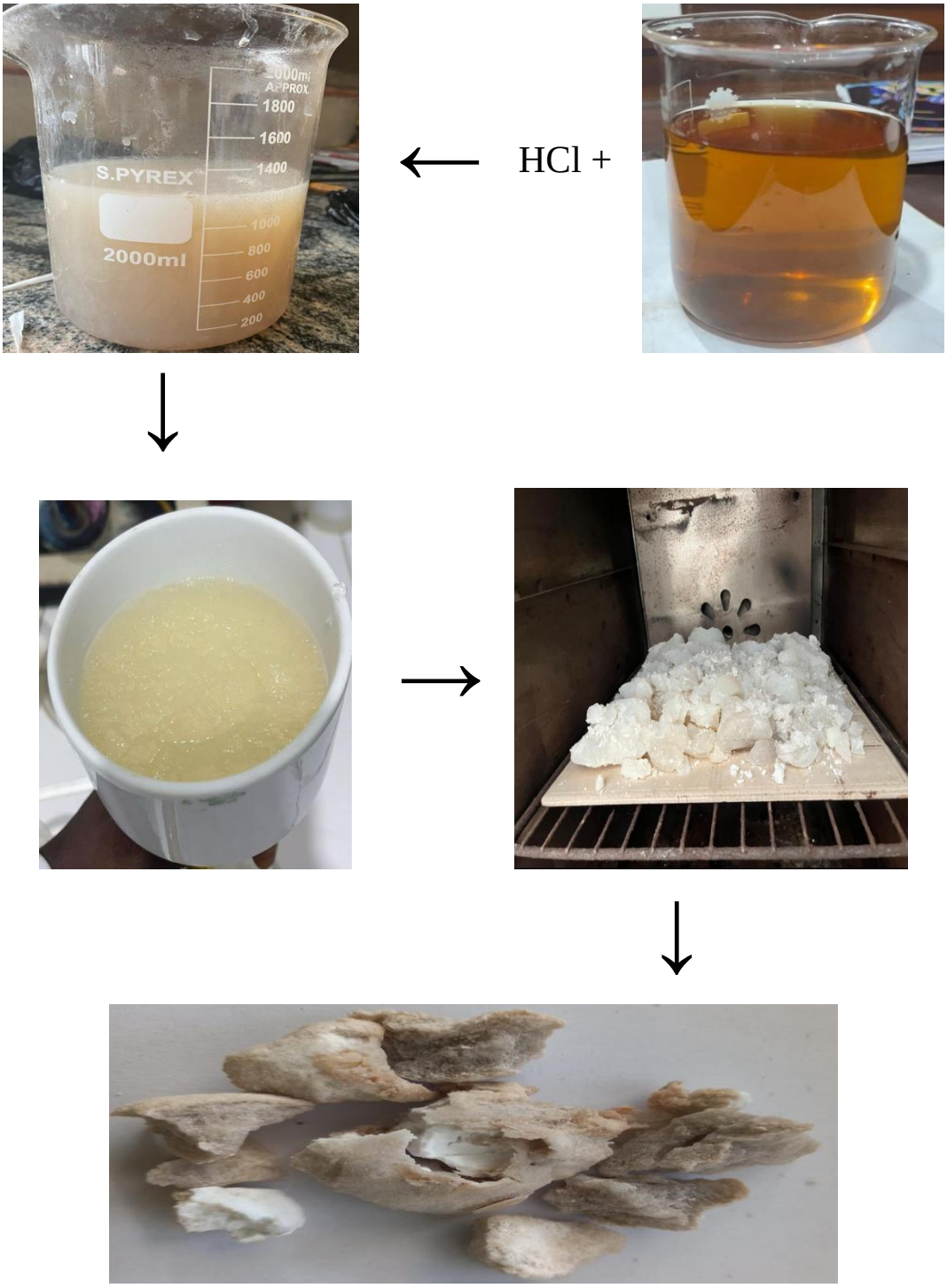

Plate 1: Stepwise extraction of Silica from the mineralised Rice Husk

Elemental Composition of the Miniralised Rice Husk and Periwinkle Shell

The silicon content, the primary element for silica production within the husk (Tables 2.1a-e), was found to be highest in all the mineralized rice husk samples (Sawasdee and Pisutpaisal, 2022; Nzereogu et al., 2023). This characteristic made them ideal for silica extraction, which is subsequently used to produce the various experimental glass samples. The mineral content from the stale (stored) rice husks and the thermomechanically dehusked samples showed slightly higher values of 10.30% and 10.33% wt., respectively,

compared to the 9.38% wt. from the mechanically dehusked samples. This variation may be due to a reduction in organic matter in the stale and thermomechanically dehusked samples. This reduction could be attributed to the degradation process in the stored husks and the potential removal of organic matter through hot water treatment in the thermomechanically dehusked samples (Bandara et al., 2020; Moura et al., 2018).

Aluminum, iron, and potassium also exhibited high values in all mineralized samples, with potassium being notably high in the thermomechanically dehusked sample (Adamu et al., 2023). These elements are common soil components, and their varying concentrations could be a result of the specific cultivation area (Bilo et al., 2015). The high potassium value may be linked to its critical role in plant growth and development, including photosynthesis, root growth, and water regulation (White et al., 2022). The presence of aluminum is likely due to its abundance as an element in the Earth's crust (Alloway, 2013). Iron, also a common soil component, is known to transport nutrients from the soil to plants (Zhang et al., 2021; Alloway, 2019). The elemental composition of the silica extracted from the mineralized rice husk samples followed a similar trend, with silicon values of 5.12% and 5.29% wt for the mechanically and thermomechanically dehusked samples, respectively.

This indicated the appropriateness of this extracted silica in the production of glass (Singh et al., 2020; Madhu et al., 2022). The high value obtained, in comparison to the value from the mineralized rice husk, may be attributed to its purity after the removal of unwanted organic and some inorganic substances (Bakar et al., 2016; Ali et al., 2021). It was observed that aluminum, sulfur, and iron were present in relatively high but still lesser amounts than the essential silicon. The greater percentage of sulfur in the extracted silica from the mechanically dehusked samples (1.13% wt) compared to the thermo-mechanically dehusked samples (0.64% wt), as shown in Table 2.1d and 2.1e, could be due to the breaking of S-OH linkages in the lignin during partial disintegration by hot water (Kumar et al., 2021; Hassan et al., 2023). A similar high silica value was found in the stale sample, which correlates with the silicon content observed in its mineralized rice husk sample in Table 2.1d. The periwinkle shell powder was considered suitable for glass production due to its exceptionally high value of about 31.05% wt calcium in the oxide form (Table 2.1f), which is a primary component in glass manufacturing (Nwanya et al., 2021; Oladele et al., 2023). The presence of sulfur may be a result of the proteinous nature of the animal mass that must have interacted with the periwinkle shell (Okoro et al., 2019).

Table 2.1a: Elemental Composition of Mineralised Mechanically Dehusked Sample

Element	Intensity	Content (%W)
sAl	0.0026	0.8195
Si	0.0897	9.3686
P	0.0080	0.3765
S	0.0052	0.3608
K	0.0133	1.0804
Ca	0.0077	0.1340
Ti	0.0002	0.0000
V	0.0000	0.0000
Cr	0.0000	0.0000

Mn	0.0017	0.1178
Co	0.0001	0.0000
Fe	0.0066	0.7084
Ni	0.0018	0.1084
Cu	0.0032	0.0764
Zn	0.0092	0.2711
As	0.0002	0.0000
Pb	0.0000	0.0000
W	0.0013	0.4873
Au	0.0000	0.0000
Ag	0.0006	0.0117
Rb	0.0117	0.1342
Nb	0.0004	0.0025
Mo	0.0094	0.2535
Cd	0.0000	0.0000
Sn	0.0166	3.3813
Sb	0.0239	3.0068

Table 2.1b: Elemental Composition of Mineralized Thermo-mechanically Dehusked Rice Husk Sample

Element	Intensity	Content (%W)
Mg	0.0002	0.2876
Al	0.0029	0.9165
Si	0.0982	10.3296
P	0.0130	0.6171
S	0.0071	0.5210
K	0.0213	1.7298
Ca	0.0154	0.3083
Ti	0.0000	0.0000
V	0.0000	0.0000
Cr	0.0000	0.0000
Mn	0.0015	0.1047
Co	0.0000	0.0000
Fe	0.0092	0.9518
Ni	0.0007	0.0390
Cu	0.0027	0.0786
Zn	0.0072	0.2496
As	0.0002	0.0000
Pb	0.0001	0.0013
W	0.0002	0.0545
Au	0.0000	0.0000
Ag	0.0006	0.0124
Rb	0.0089	0.0938
Nb	0.0000	0.0000
Mo	0.0048	0.1493

Cd	0.0003	0.0004
Sn	0.0124	2.4666
Sb	0.0184	2.3196

Table 2.1c: Elemental Composition of Mineralized Stale Rice Husk Sample

Element	Intensity	Content (%W)
Mg	0.0000	0.0000
Al	0.0024	0.7615
Si	0.0980	10.3050
P	0.0058	0.2750
S	0.0048	0.3257
K	0.0070	0.5613
Ca	0.0067	0.1102
Ti	0.0000	0.0000
V	0.0000	0.0000
Cr	0.0000	0.0000
Mn	0.0011	0.0762
Co	0.0002	0.0039
Fe	0.0083	0.8704
Ni	0.0021	0.1261
Cu	0.0037	0.1399
Zn	0.0130	0.2878
As	0.0006	0.0000
Pb	0.0000	0.0000
W	0.0017	0.6640
Au	0.0000	0.0000
Ag	0.0000	0.0000
Rb	0.0061	0.0559
Nb	0.0000	0.0000
Mo	0.0081	0.1982
Cd	0.0000	0.0000
Sn	0.0154	3.1277
Sb	0.0228	2.8672

Table 2.1d: Elemental Composition of Silica Obtained from Mechanically Dehusked Rice Husk Sample

Element	Intensity	Content (%W)
Mg	0.0000	0.0000
Al	0.0016	0.4990
Si	0.0509	5.1206
P	0.0047	0.2199
S	0.0142	1.1295
K	0.0031	0.2419
Ca	0.0023	0.0304
Ti	0.0000	0.0000

V	0.0001	0.0052
Cr	0.0002	0.0037
Mn	0.0002	0.0055
Co	0.0000	0.0000
Fe	0.0026	0.3282
Ni	0.0022	0.1353
Cu	0.0033	0.0639
Zn	0.0064	0.2225
As	0.0003	0.0000
Pb	0.0004	0.0131
W	0.0006	0.2058
Au	0.0000	0.0000
Ag	0.0000	0.0000
Rb	0.0038	0.0235
Nb	0.0000	0.0000
Mo	0.0034	0.1920
Cd	0.0000	0.0000
Sn	0.0198	4.1009
Sb	0.0290	3.6513

Table 2.1e: Elemental Composition of Silica Obtained from Themo-mechanically Dehusked Rice Husk Sample

Element	Intensity	Content (%W)
Mg	0.0000	0.0000
Al	0.0015	0.4654
Si	0.0526	5.2942
P	0.0020	0.0920
S	0.0084	0.6350
K	0.0030	0.2389
Ca	0.0026	0.0349
Ti	0.0000	0.0000
V	0.0001	0.0071
Cr	0.0001	0.0012
Mn	0.0000	0.0000
Co	0.0000	0.0000
Fe	0.0025	0.3197
Ni	0.0020	0.1217
Cu	0.0038	0.1519
Zn	0.0055	0.1905
As	0.0002	0.0000
Pb	0.0005	0.0163
W	0.0005	0.1459
Au	0.0000	0.0000
Ag	0.0001	0.0030
Rb	0.0032	0.0148

Nb	0.0000	0.0000
Mo	0.0054	0.1313
Cd	0.0000	0.0000
Sn	0.0192	3.9724
Sb	0.0291	3.6710

Table 2.1f: Elemental Composition of The Pulverised Periwinkle Shell Powder

Element	Intensity	Content (%W)
Mg	0.0000	0.0000
Al	0.0008	0.2444
Si	0.0034	0.2493
P	0.0054	0.2523
S	0.0085	0.6418
K	0.0000	0.0000
Ca	0.3188	31.0508
Ti	0.0000	0.0000
V	0.0001	0.0056
Cr	0.0001	0.0026
Mn	0.0001	0.0031
Co	0.0000	0.0000
Fe	0.0043	0.4894
Ni	0.0014	0.0839
Cu	0.0023	0.0609
Zn	0.0039	0.1335
As	0.0001	0.0000
Pb	0.0003	0.0070
W	0.0003	0.0978
Au	0.0000	0.0000
Ag	0.0000	0.0000
Rb	0.0002	0.0009
Nb	0.0000	0.0000
Mo	0.0037	0.1817
Cd	0.0000	0.0000
Sn	0.0106	2.0605
Sb	0.0158	1.9907

Glass Production

The production of the experimental glass samples followed a modified conventional method in which silica extracted from rice husks and calcium oxide derived from pulverized periwinkle shells replaced the traditional raw materials, while sodium carbonate (Na_2CO_3) served as the fluxing agent (*Scholes, 2011; Shelby, 2005*). The extracted silica was reduced to fine particulate form and mixed with periwinkle shell powder and Na_2CO_3 in a ratio of 4.7:1:1. The mixture was homogenized by dry-mixing to ensure uniform dispersion of components before being transferred into a preheated graphite crucible. Melting was

conducted in a furnace at 1300 °C for one hour, yielding a homogeneous molten glass (*Varshneya et Mauro, 2019*). The molten material was then poured into a mould, cooled, and subsequently quenched (Plate 2) to obtain the final glass samples.

$$SiO_2 + Na_2CO_3 + CaCO_3 \longrightarrow Na_2O.\ CaO.\ xSiO_2 + 2CO_2$$

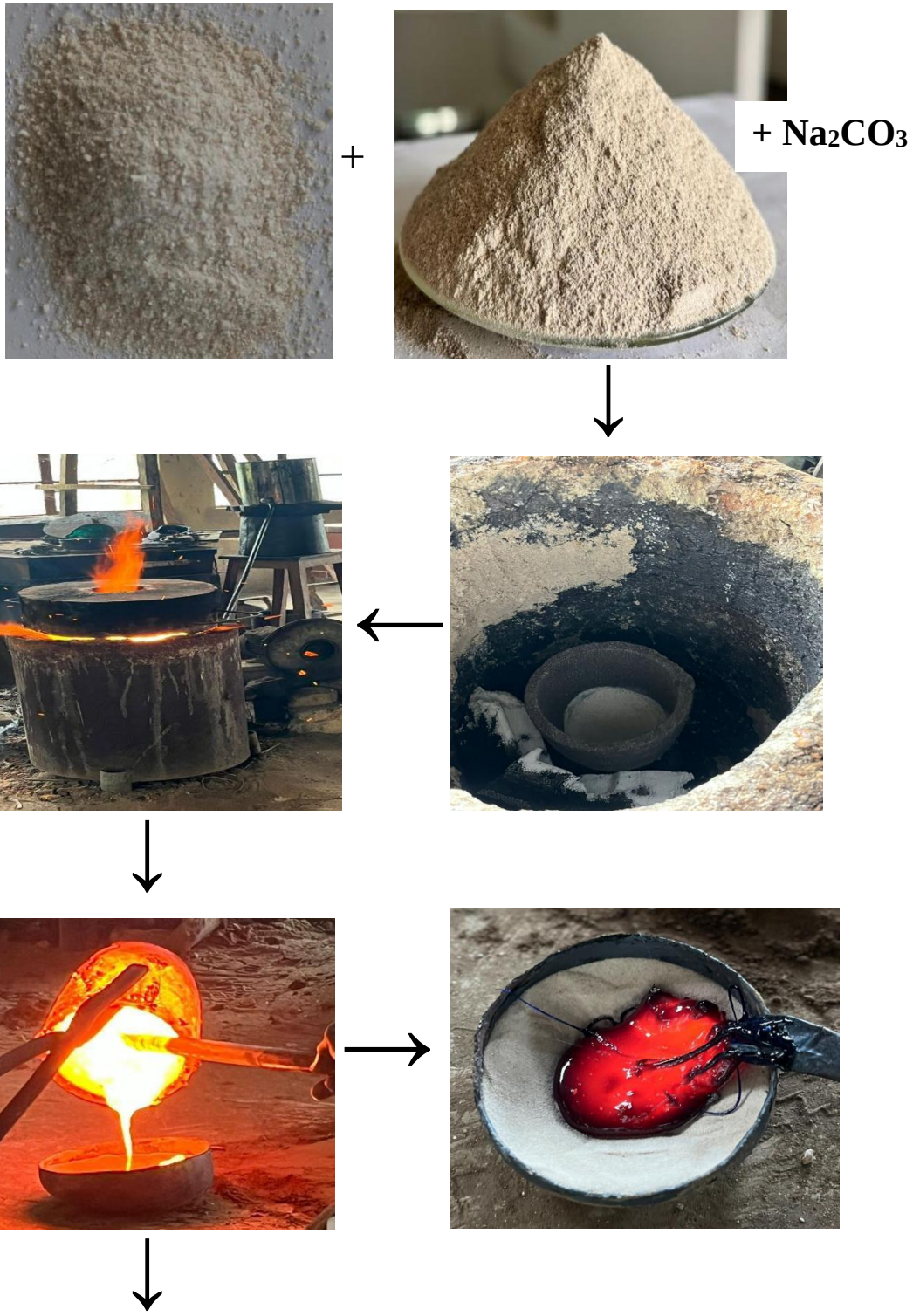

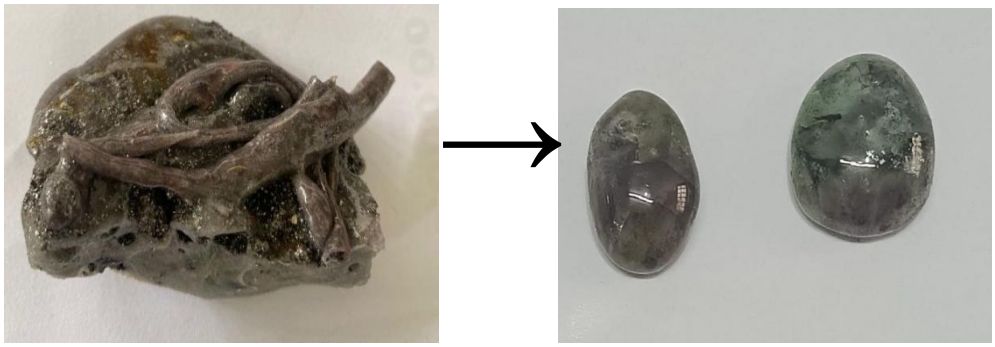

Plate 2: Production of Experimental Glass Samples

The above description was utilized for the production of the metal doped glass samples with a slight modification. An appropriate amount of the metal salts was weighed differently and added to the extracted silica, pulverised periwinkle shell powder and sodium carbonate, after which they were further dry mixed before transferring them into the preheated graphite crucible pot. The summary of the components and the mixing ratio of the produced glass is presented in Table 2.2 while the produced transition metal doped glasses are presented in Figures 5 to 8.

Table 2.2: Combining Ratio of Components in the Produced Glass Samples

Components	Combining Ratio (%)
Silica + Periwinkle + Na_2CO_3	70:15:15
Silica + Periwinkle + Na_2CO_3 + Fe^{3+} ions	69:15:15:1
Silica + Periwinkle + Na_2CO_3 + Co^{2+} ions	69:15:15:1
Silica + Periwinkle + Na_2CO_3 + Cu^{2+} ions	69:15:15:1
Silica + Periwinkle + Na_2CO_3 + Ni^{2+} ions	69:15:15:1

Figure 5: Co^{2+} Ion Doped Glass

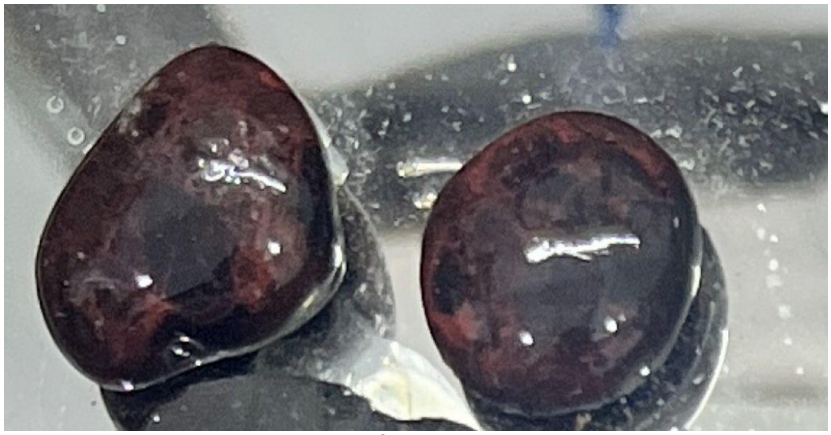

Figure 6: Cu^{2+} Ion Doped Glass

Figure 7: Ni^{2+} Ion Doped Glass

Figure 8: Fe^{3+} Ion Doped Glass

RESULTS AND DISCUSSION

Proximate Analysis

The proximate composition of the different rice husk samples as contained in Table 3.1 showed variation in the observed characteristics of the different samples.

Table 3.1: Proximate Composition of the Different Rice Husk Samples

Samples	Parameters (%)					
	Moisture	Ash	Crude Fibre	Ether Extract	Crude Protein	Carbohydrate
Mechanically Dehusked	6.41	13.80	28.47	5.72	9.41	38.17
Thermo-Mechanically Dehusked	7.25	17.37	21.88	11.80	12.47	29.23
Archived/ Stored	6.63	30.59	23.77	0.98	10.94	27.09

Carbohydrate content followed the expected trend: the stale husk exhibited the lowest value (27.09%), followed by the thermomechanically dehusked (29.23%), while the mechanically dehusked had the highest (38.17%). The reduced carbohydrate levels in the stale sample were attributed to microbial degradation of cellulosic sugars by fungi (*Lynd et al., 2002; Kubicek et al., 2014*). The higher content in the fresh, mechanically dehusked husk was linked to intact cellulose and minimal degradation, while the reduction in the thermomechanically dehusked husk reflected partial depolymerization and dissolution of carbohydrate and lignin during hot-water treatment.

Moisture content was highest in the thermomechanically dehusked sample (7.25%) due to water absorption during processing, while the mechanically dehusked sample showed the lowest (4.43%). The stale husk recorded 6.64%, likely from moisture uptake over time, consistent with the hygroscopic nature of lignocellulosic biomass (*Kumar et al., 2009*).

Crude fibre was greatest in the mechanically dehusked husk (28.47%), reflecting higher cellulose, hemicellulose, and lignin content. The thermomechanically dehusked sample showed a reduced value (21.88%) due to partial breakdown during hot-water treatment, while the stale husk (23.77%) contained residual fibre and impurities from degradation (*Sun et al., 2000*).

Ash content was lowest in the mechanically dehusked husk (13.8%) but highest in the stale husk (30.59%), likely due to the progressive breakdown of cellulose and hemicellulose during storage, leaving behind mineral-rich residue (*Jiang et al., 2013*).

Ether extract showed significant variation: the thermomechanically dehusked sample had the highest value (11.8%), attributed to the release of lipophilic compounds (waxes, oils, and resins) during combined heat–mechanical processing (*AOAC, 2019; Nwosu et al., 2014*). The mechanically dehusked husk had a moderate content (5.72%) consistent with natural lipid levels in fresh husks (*Adejumo et al., 2011*), while the stale husk showed the lowest (0.98%) due to microbial degradation and volatilization during extended storage (*Nwokocha et al., 2012; Onwuka, 2018*).

Fourier Transform Infrared Spectroscopic Analyses

The IR spectral analysis of both the raw materials and the produced glass samples (Table 3.2) revealed a distinct –OH band at 3384 cm^{-1} in the extracted silica, attributed to residual lignin from the rice husk ash and the formation of Si–OH groups (*Capeletti and Zimnoch, 2016*). These OH bands disappeared in the produced glass samples, indicating bond reorganization during glass formation in both doped and undoped systems. Broad absorptions at 2322–2563 cm^{-1} in all glass samples were associated with Si–OH overtone bands linked to moisture. A slightly higher shift to 2363 cm^{-1} in Co^{2+}-doped glass suggested reduced water coordination, reflecting the relative stability of the Co^{2+} (d^7) configuration compared to the less stable Ni^{2+} (d^8) and Cu^{2+} (d^9) states, which required electron donation from water molecules (Eldaly et al., 2022).

Table 3.2: Infra-red Absorption Bands for the Raw and Produced Glass Samples (cm^{-1})

Silica	Periwinkle Shell	Flint	Flint + Co^{2+} ions	Flint + Ni^{2+} ions	Flint + Cu^{2+} ions	Flint + Fe^{3+} ions	Tentative Band Assignments
3384						3750	Free —OH Stretch / isolated Si—OH / molecular H_2O
2322	2360	2359	2363	2323	2343 2324	2363	Overtones in the silica matrix (water related Si—OH bands) Asymmetric Stretch
2166		2166					CO_2 Overtone
1983							Combination of overtone bands
1651							H—O—H Bending Vibration
1457							C—O Stretching of CO_3^{2-}
	1454						Asymmetric Carbonate vibration
	1081						Symmetric vibration of carbonate
	1036.2						Asymmetric Phosphate vibration
1014							Si—O Asymmetric vibration
		932	936	930	930	928	Si—O—Si Stretch (Non-bridging Oxygen)
	857						Carbonate (in-plane) bending vibration
		764	768	768	766	760	Si—O—Si Stretch (Bridging Oxygen)
		671					CO_2 Bending (Gas Phase)
					643		Cu-O vibration (Cu_2O type)
	626						Phosphate bending/ Ca-O) vibration
				624			P—O (Phosphate bending/ Ca—O vibration
		619	619				Co—O Stretching in tetrahedral CoO_4 (Co^{2+}—O) PO_4^{3-} / bend in Calcium Phosphate
					610		Cu—O vibration and / or Ca—O/ P-O bending
		592			587		Ca—O Stretching/ PO_4^{3-} bending
	582						Secondary Phosphate bending
				572			Ca—O Stretching
						563	Fe—O Stretching
			559				Co—O stretching in octahedral CoO_6 (Co^{3+}— O)
					552		Cu—O (in CuO/Cu_2O) Stretch
				503			Si—O—Si bending with minor Mg/Ca—O overlap
						514	Fe—O (hematite) stretching/ Si—O—Si (O—Si—O) bending
492							Si—O—Si Secondary bending

		477					Si—O—Si bending (Amorphous SiO_2)
462							Si—O—Si bending in silicate network
					457		S—O—Si bending in silicate network
	440						Ca—O / Mg—O vending vibration
			436				Na/Ca—O vibration / O—Si—O bending
429							Si—O—Si Rocking bending
						425	Fe—O Stretching (Fe_2O_3 / Fe_3O_4)
				421			Ni—O Stretching and Si—O—Si bending
					418		Cu—O stretching and Si—O bending overlap

Carbonate-related C–O bands at 1457 and 1454 cm^{-1} were present in the silica and periwinkle shell, respectively, but disappeared in the produced glasses. This indicates possible participation of carbonate groups in network bond formation, contributing to the crystallinity of the final products. In the fingerprint region (764–926 cm^{-1}), several Si–O–Si bridging and non-bridging bonds were observed, confirming the suitability of extracted rice husk silica as a replacement for conventional sand-based silica (*Ellerbrock et al., 2024*).

Characteristic metal–oxygen (M–O) vibrations were also identified (Leong et al., 2014). Co^{2+} doped samples exhibited Co–O bands at 642 cm^{-1} (Cu_2O-type coordination), 619 cm^{-1} (tetrahedral CoO_4), and 559 cm^{-1} (octahedral CoO_6), suggesting the coexistence of multiple geometries. Similarly, Cu^{2+} showed Cu–O absorption at 610 cm^{-1}, while Ni^{2+} and Cu^{2+} doped glasses exhibited P–O bending vibrations near 624–587 cm^{-1}, consistent with phosphate-type glass structures (*Adegbola et al., 2024*).

The Fe^{3+} ion doped glass also showed the possibility of its existence in multiple or various oxidation states by forming the Fe–O bonds in the form of Fe_2O_3 (+3 state) and Fe_3O_4 which existed in the $FeO.Fe_2O_3$ thus exhibiting the +2 and +3 oxidation states at 425 cm^{-1} *(Leong et al.,2014)*.

The undoped flint glass also displayed weak M–O absorptions, attributable to trace metals present in the raw materials. Collectively, the spectra confirmed that Si–O coordination dominated the glass network, while transition-metal ions contributed unique structural modifications through M–O bonding.

Ultraviolet-Visible Spectroscopic (UV- VIS) Absorbance of Glass Samples

The UV–Vis spectrum of flint glass (Fig. 9) displayed a nearly flat absorbance profile between 400–900 nm, indicating minimal absorption in the visible region, which is typical of undoped flint glass (*Varshneya et Mauro, 2019*). The absence of distinct peaks confirmed the lack of transition-metal doping, while a sharp transmittance rise near 400 nm and drop around 550 nm reflected impurity interactions within the amorphous matrix (*Rawson, 1980*). The baseline absorbance range of 1.4–1.7 was attributed to intrinsic thickness and baseline absorption (*Bingham et Handke, 1992*).

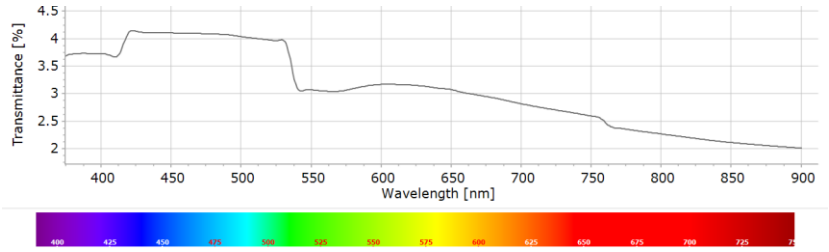

Figure 9: Flint Glass Spectrum

The Ni^{2+} ion-doped glass spectrum (Fig. 10) exhibited high absorbance (~3.1) at 400 nm, followed by a decline to a plateau between 450–600 nm, and then a gradual increase to ~2.9 at 900 nm. This profile is characteristic of Ni^{2+} ions (*Schreiber et al., 2007*). Strong absorption below 450 nm corresponded to charge-transfer d-d transitions (*Bingham et Handke, 1992*). The flat 450–600 nm region indicated weaker overlapping transitions, while the rise beyond 600 nm was consistent with the $^3A_2g(F) \rightarrow {}^3T_2g(F)$ transition, which explained the green hue of the glass. Transmittance peaks between 500–600 nm indicated transmission of green and yellow light, consistent with Ni^{2+}/Ni^{3+} overtone transitions (*Pisarski et al., 2010*).

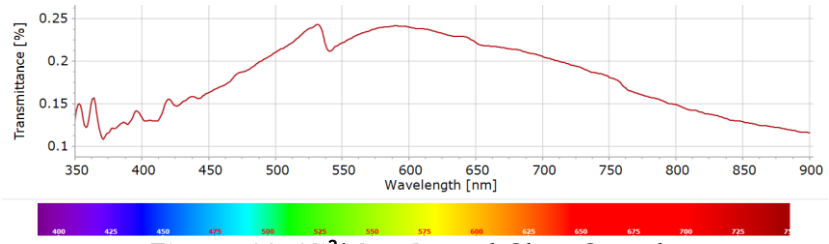

Figure 10: Ni^{2+} Ion Doped Glass Sample

The Cu^{2+} ion-doped glass spectrum (Fig. 11) was broad and weak, showing a gradual absorbance decline from ~0.44 at 400 nm to ~0.34 at 900 nm. This profile reflected a disordered matrix and a high proportion of Cu^{+} ions, with fewer Cu^{2+} ions present. A minor peak near 450 nm in the transmittance spectrum suggested d-d transitions of Cu^{2+} ions at low concentration (*Bingham et Handke, 1992; Varshneya et Mauro, 2019; Dutta et Ghosh, 2015*). The absorbance pattern corresponded with the observed bluish-green coloration.

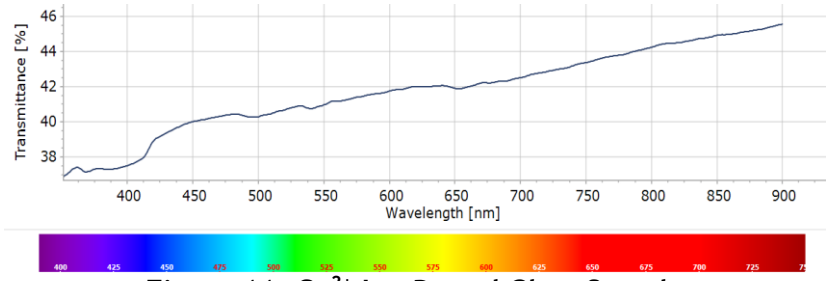

Figure 11: Cu^{2+} Ion Doped Glass Sample

The Co^{2+}ion-doped glass spectrum (Fig. 12) displayed a broad band with a peak around 415–450 nm, characteristic of Co^{2+} electronic transitions such as $^4T_1g(F) \rightarrow {}^4T_1g(P)$ (*Duffy, 1990; Pisarski et al., 2010*). The lack of sharp features indicated a disordered glass environment (*Rawson, 1980; Shelby, 2005*). The declining absorbance beyond 500 nm signified weaker absorption in the red region, consistent with the observed blue-green coloration due to preferential absorption of yellow-red light. Transmittance in the 400–500 nm range further confirmed blue light transmission associated with Co^{2+} ions (*Bingham et Handke, 1992*).

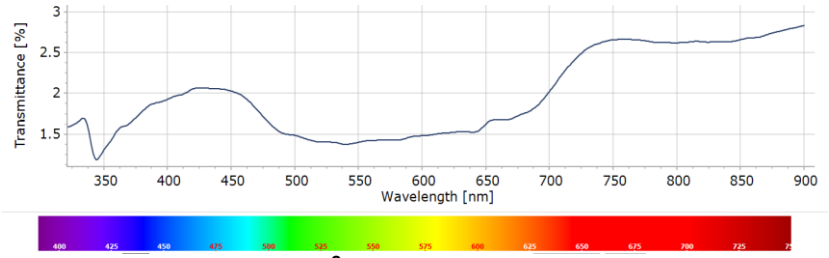

Figure 12: Co^{2+} Ion Doped Glass Sample

The spectrum of the iron-doped glass (Fig. 13) showed a decrease in absorbance from approximately 2.4 at 400 nm to a minimum of about 1.6-1.7 between 500-600 nm, followed by an increase to about 2.2 at 900 nm. This pattern indicates the presence of both Fe^{2+} and Fe^{3+} ions. The initial drop in absorbance may be the final portion of a strong UV absorption band, such as charge transfer transitions from O^{2-} to Fe^{3+} (*Duffy, 1990; Fuxi, 1992*). The flat region between 500-600 nm suggests weaker d-d transitions, such as $5T_{2g} \rightarrow 5Eg$ for Fe^{2+} (*Stebbins and Xiao, 1999*). The rise in absorbance beyond 600 nm is likely characteristic of Fe^{2+}, which often has broad absorption bands in this region. Depending on the ratio of Fe^{2+} to Fe^{3+}, the glass may have a greenish or brownish hue (*Toby and Cottrell, 2012*). The transmittance peaks at 500-550 nm and 570-650 nm corresponded to the transmission of green and yellow-brown light, respectively, which are associated with transitions of Fe^{2+} and Fe^{3+} ions (*Wright, 2014*).

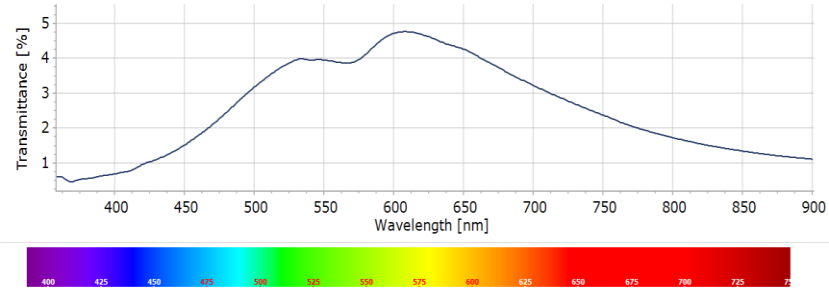

Figure 13: UV-visible of the Fe^{3+} Ion Doped Glass Sample

Physical Measurements

The strength and stability of the produced glass samples and the effects of the transition metal additives on these properties as presented as Modulus are presented in Table 3.3 are discussed as follows

Table 3.3: Summary of the Modulus Tests Results of the Produced Glass Samples

Sample	Hardness (BHN)	Elongation at Break (mm)	Strength (MPa)	Compressive Strength (Geometry Based) (MPa)	Stiffness (MPa)
Flint	156.50	1.67	36.09	21.75	1601.59
Co^{2+} ion Doped	130.00	1.81	25.85	25.86	1135.58
Cu^{2+} ion Doped	63.00	0.56	8.62	0.00	0.00
Ni^{2+} ion Doped	80.00	1.76	27.08	18.11	1322.25
Fe^{3+} ion Doped	84.50	1.42	33.60	29.00	1380.86

Hardness

The localized plastic deformation measurements revealed that the flint (undoped) glass exhibited the highest hardness value (156.50 BHN) compared to the transition metal-doped samples. This superior hardness is attributed to its structural characteristics, particularly the absence of chelate-forming transition metals that were present in the doped variants. While elemental analyses confirmed the presence of metals in the raw materials, the lower degree of crystallinity in the flint glass allowed it to better resist applied force prior to failure. This observation supports the inverse relationship between crystallinity and hardness, whereby increased crystallinity reduces a material's resistance to deformation (*Wang, 2005*).

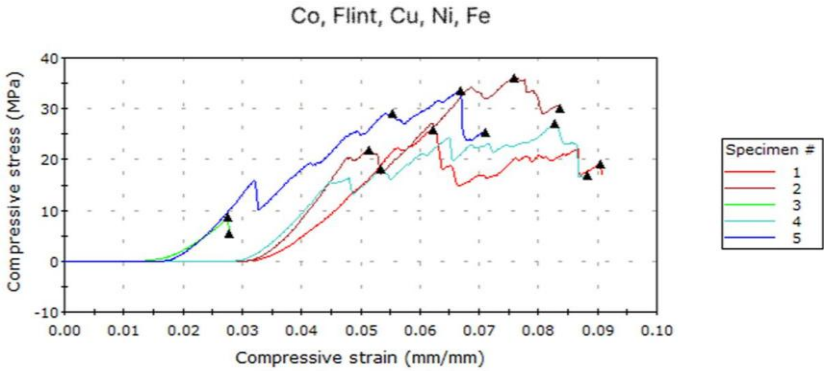

Figure 14: Compressive Stress-Strain Curve of the Produced Experimental Glass Samples

Where: 1, 2, 3, 4 and 5 are Co^{2+}, Flint, Cu^{2+} Ni^{2+} and Fe^{3+}ion-doped glass samples respectively.

The elevated hardness of the flint glass could be attributed to its mixed crystalline and semi-crystalline phases, which enhance both hardness and strength. Its amorphous features, confirmed by SEM analysis, also contributed to this mechanical performance.

Among the transition-metal-doped samples, the Co^{2+}ion-doped glass exhibited the highest hardness. This was linked to the coexistence of octahedral (CoO_6) and tetrahedral (CoO_4) geometries associated with the Co^{2+} ion in its d^7 configuration, as indicated by the IR spectra (Table 3.2). Despite containing fewer M–O bonds compared to the other doped glasses, the bond network formed by these geometries, combined with its relatively higher semi-crystalline character, reduced its overall crystallinity and improved its ability to resist deformation.

In contrast, the Cu^{2+}-doped glass exhibited the lowest hardness. This weakness was attributed to the coexistence of +1 and +2 oxidation states, which promoted extensive bond formation within the glass matrix. The resulting high crystallinity reduced hardness, consistent with the inverse relationship between crystallinity and resistance to deformation (*Wu and Peng, 2018*). Additionally, the instability of the d^9 configuration likely compromised structural stability, further diminishing hardness. Similarly, the Ni^{2+}-doped glass exhibited reduced hardness compared to Co^{2+} due to its higher crystallinity.

Overall, all transition-metal-doped glasses demonstrated lower hardness values than flint glass, primarily due to their increased crystallinity and denser bond networks arising from complex formation. Also, the high level of crystallinity of the Cu^{2+}, Ni^{2+}, and Fe^{3+} ion doped glass samples as compared to the Co^{2+} ion doped made the former exhibit lower hardness (*Eldaly et al., 2022*).

Elongation at Break

The elongation at break, which reflects the ductility of a material, showed that the Co^{2+}ion-doped glass possessed the highest ductility among the transition metal-doped samples. This behavior may be attributed to its relatively low crystallinity, as confirmed by Scanning Electron Microscopy results, which provided a balance of crystalline and semi-crystalline phases capable of distributing applied stresses and enhancing dimensional stability.

In contrast, the Cu^{2+}-doped glass exhibited the lowest elongation at break (0.56 mm). Its poor ductility could be due to the instability of its structure, coupled with a high density of metal–oxygen (M–O) bonds that promoted excessive crystallinity and hindered elastic recovery (*Chavan et Sreenivasulu, 2021*). The flint glass displayed a slightly reduced elongation value (1.67 mm) compared to Co^{2+} doping, which may be attributed to microstructural porosity caused by trapped gases such as CO_2 during production. The presence of these voids likely compromised its overall ductility (Khadraoui *et al., 2024*).

Strength

The maximum compressive strength of the produced glass samples followed the same trend as the hardness values, reflecting the cumulative ability of materials to withstand stress without failure. While strength represents the bulk resistance to applied stress and strain, hardness reflects resistance to localized deformation (*Egami et al., 2013*). The direct correlation observed between these two parameters may be due to the high degree of homogeneity achieved during mixing, which ensured near-uniform distribution of the constituent components both within and across the glass matrices especially the added metal ions. This was further supported by Energy Dispersive X-ray Spectroscopy results for

the produced experimental glass samples (Fig.15), which confirmed an almost equal distribution of elemental ions across different regions of the samples (*Sallam et al., 2020*). Such uniformity was facilitated by the initial dry-mixing process carried out prior to smelting, which promoted consistency in the microstructure and, consequently, in the mechanical properties of the glass.

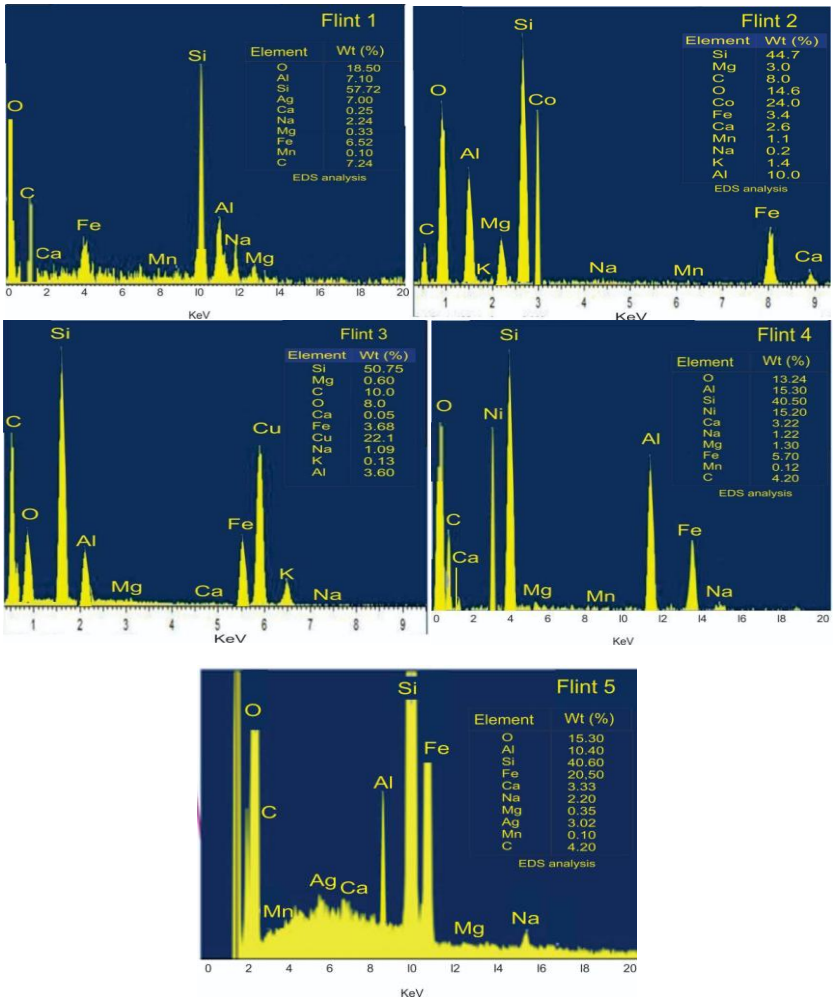

Figure 15: Energy Dispersive Spectra of the Produced Glass Samples.

Legend:

- Flint 1: Undoped Glass Sample
- Flint 2: Co^{2+} Ion Doped Glass Sample
- Flint 3: Cu^{2+} Ion Doped Glass Sample
- Flint 4: Ni^{2+} Ion Doped Glass Sample
- Flint 5: Fe^{3+} ion Doped Glass Sample

Compressive Strength

The compressive strength, expressed as the compressive stress at yield, provided a geometry-based measure of the cumulative strength of the composites (*Yin, 2013*). Unlike the observed trend in the hardness, the compressive strength trends differed among the produced glasses, reflecting the influence of lattice geometries introduced by transition metal doping. According to the Random Network Theory, glass is primarily composed of disordered SiO_4 tetrahedral interconnected within an amorphous framework (*Huheey, Keiter, et Keiter, 1997; Egami et al., 2013*). The structure of the undoped flint glass largely conformed to this model, with slight deviations caused by minor impurities (*Vercamer et al., 2015*).

The flint glass exhibited a compressive strength of 21.75 MPa, which was lower than that of the Co^{2+}-doped glass (25.86 MPa). The improved performance of the cobalt-doped sample was attributed to the formation of a tetragonally distorted octahedral complex that strengthened the network, as supported by UV–Visible absorption features (*Elbashar et al., 2020*).

In contrast, the Ni^{2+}-doped glass showed a lower geometric strength of 18.11 MPa, likely due to the weaker stability of the Ni^{2+} octahedral geometry compared to its preferred square planar configuration. This reduced the stability of the glass network, consistent with the lower stability of the d^8 configuration relative to the d^7 (Co^{2+}) and d^5 (Fe^{3+}) states (*Eldaly et al., 2022*).

The Cu^{2+} ion-doped glass exhibited the weakest compressive strength, which was linked to its high crystallinity and the inherent instability of the d^9 configuration. Although capable of forming an octahedral complex, this unstable electronic configuration hindered the formation of a robust glass network, thereby reducing its overall geometric strength. The highest geometric strength was observed in the Fe^{3+} doped glass, and this could be attributed to the chelate formation that resulted in mainly the octahedral geometry for the Fe^{3+} and Fe^{2+} ions in the form of Fe_2O_3 as expressed in the equilibrium equation below

$$Fe_3O_4 \rightleftharpoons FeO{\cdot}Fe_2O_3$$

which resulted in a greater network formation and increased geometrical strength that was improved upon by the stability of Fe^{3+} that has a stable d^5 configuration *(Choudhary and Singh, 2016)*.

A stable configuration is susceptible to the formation of a metal complex, so the low stability of the d^9 configuration of the Cu^{2+} ion may be responsible for the weak network structure formed within the glass, despite forming an octahedral complex with the glass molecule. The weak octahedral structure formed in the glass matrix may be due to the low Crystal Field Stabilization Energy (CFSE) as compared with that of the d^5 of the Fe^{3+} ion *(Chavan and Sreenivasulu, 2021)*.

Stiffness

The stiffness (E-modulus), representing the resistance of the glass to elastic deformation under stress, was highest in the undoped flint glass. This superior resistance is attributed to its relatively higher amorphous content, which enabled effective distribution of applied stresses within the amorphous phase surrounding its crystalline domains (*Varshneya and Mauro, 2019; Egami et al., 2013*).

In contrast, the Cu^{2+} ion-doped glass exhibited negligible stiffness due to its high crystallinity and structural instability. The extensive M–O bonding network within its matrix enhanced crystallinity but reduced its capacity to disperse applied stresses, resulting in brittleness (*Wu and Peng, 2018; Mekki and Salim, 1999*).

The Co^{2+} ion-doped glass displayed a lower stiffness value (1135.58 MPa) compared to its relatively higher strength, hardness, and ductility. This anomaly may be explained by the coexistence of CoO_4 tetrahedral and CoO_6 octahedral geometries, as indicated by IR spectra (Table 4.3). These structural distortions are known to lower stiffness in materials (*Eldaly et al., 2022; Leong et al., 2014*). Additionally, the presence of alkali and alkaline earth elements such as Na and Ca, detected by SEM–EDS, likely further reduced the stiffness of the Co^{2+} ion-doped glass (*Shelby, 2005; Egami et al., 2013*).

The similar E-modulus values of 1322.25 MPa and 1380.86 MPa for the nickel ion (Ni^{2+}) and iron ion (Fe^{3+}) doped glass samples, respectively, may be due to the octahedral geometry present in both. The slightly lower value in the Ni^{2+} doped glass may be caused by a distorted octahedral geometry, which is known to be less stable and slightly weaker than the normal octahedral complex found in the Fe^{3+} ion doped glass *(Cotton et al., 1999; Choudhary and Singh, 2016)*.

Scanning Electron Microscopy

The scanning electron micrographs (SEMs) of the glass samples revealed distinct variations in both surface and internal microstructures across different magnifications (Fig. 15). The flint glass exhibited a high degree of semi-crystallinity, consistent with the structure of conventional undoped glass, suggesting good compatibility between its constituent components. The observed features corresponded to the mechanism of surface crystal nucleation, which is known to enhance mechanical properties (*Egami et al., 2013; Varshneya et Mauro, 2019*). Additionally, small bubble bands (pores) were detected within the flint sample. Such pores might be associated with the reduced volume gaps in the glass matrix that contributed to the improved layer strength (*Goldstein et al., 2017*). These bubbles likely originated from the CO_2 release during the decomposition of periwinkle shells as represented in the equation below.

$$CaCO_3 \rightarrow CaO + CO_2$$

Their presence was linked to the hardness and strength of the flint glass (*Okonkwo et Odiong, 2016*). In contrast, the Ni^{2+}-doped glass displayed a larger number of pores, including smaller pores embedded within larger ones. This morphology weakened the structure of the sample, as increasing pore size led to thinner walls between voids, thereby lowering its ability to resist applied compressive forces (*Egami et al., 2013*).

The Co^{2+} and Cu^{2+} ion-doped glass samples both exhibited comparable levels of semi-crystallinity. Despite existing in the same oxidation state within the glass matrix, the Cu^{2+} ion-doped glass was more crystalline due to the ability of Cu^{2+} ions to accept lone pairs from donor atoms, thereby forming strong dative bonds. Its relatively large ionic radius further facilitated extensive bonding within the network. However, this increased crystallinity translated into reduced mechanical strength, as the glass became more brittle in nature (*Wu and Peng, 2018; Mekki and Salim, 1999*).

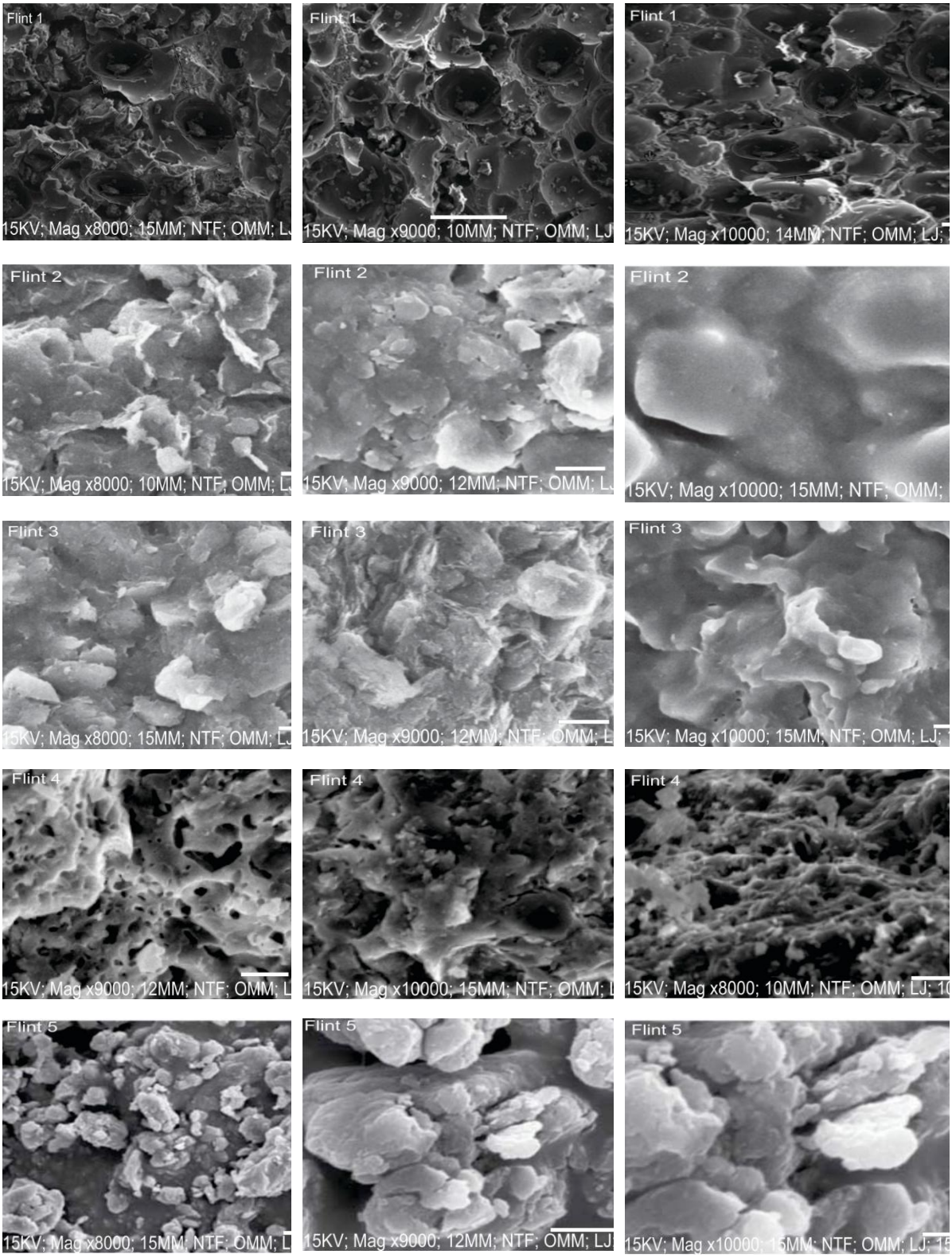

Figure 16: Scanning Electron Micrographs of the Produced Glass Samples at different magnifications

Legend

- Flint 1: Undoped Glass Sample

- Flint 2: Co^{2+} Ion Doped Glass Sample
- Flint 3: Cu^{2+} Ion Doped Glass Sample
- Flint 4: Ni^{2+} Ion Doped Glass Sample
- Flint 5: Fe^{3+} Ion Doped Glass Sample

This trend differed in the Fe^{3+} ion doped glass, where the stability of the bonds formed was responsible for the more cohesive micrograph observed (Fig. 16) where the presence of pores was invisible. This could account for the higher strength exhibited by the Fe^{3+} ion doped glass with the ability to withstand a high compressive stress than the Ni^{2+} doped ones (*Choudhary et Singh, 2016*).

CONCLUSION

This study has demonstrated the successful synthesis of glass using agricultural and marine wastes, specifically rice husks as a source of silica and periwinkle shells as a source of biogenic calcium carbonate. The incorporation of transition metal ions such as, Ni^{2+}, Cu^{2+}, Co^{2+} and Fe^{3+} ions into the glass matrix revealed significant effects on the optical and structural properties of the products. UV–Visible spectroscopy showed distinct absorption bands that were characteristic of the dopant ions, confirming their role in modifying the coloration and transparency of the glass samples. FTIR analysis verified the formation of a silicate glass network, while SEM revealed relatively smooth surfaces with minimal porosity, indicating good homogeneity of the samples. Overall, the results confirmed that rice husks and periwinkle shells can serve as viable alternative raw materials for eco-friendly glass production, reducing the common environmental pollution associated with the improper disposal of these waste while providing added value to agricultural and marine by-products and reducing the cost of an important and essential material as glass due to the extremely low cost of the basic raw materials.

REFERENCES

Adamu, G.D., Dankawu, U.M., Maharaz, M.N., Chifu, E.N., Zarma, S.S., Silkwa, N.W. and Ahmadu, M. (2023). Evaluation of Chemical Compositions of Rice Husk from Local Rice Species Using X-Ray Fluorescence Technique. *FUDMA Journal of Sciences (FJS)*, 7(4), 82–89.

Adejumo, B. A., Alakowe, A. T. and Obi. D. E. (2011). Chemical Composition and Functional Properties of Rice Husk. Journal of Agricultural Research, 5(3), 45–52.

Adegbola, A. A.; Balogun, A. O. and Okonkwo, P. C. (2024). Structural analysis of phosphate-based glasses doped with transition metals. Materials Chemistry Reports, 12(1), 88–97.

Ali, A. M. M., Ghaffar, A., Bashir, M. K., Ali, H., & Bashir, M. H. (2021). Routes for energy and bio-silica production from rice husk: A comprehensive review and emerging prospect. *Renewable and Sustainable Energy Reviews*, 149, 111358. ScienceDirect.

Alloway, B. J. (2013). Sources of heavy metals and metalloids in soils. In *Heavy Metals in Soils: Trace Metals and Metalloids in Soils and their Bioavailability* (pp. 11–50). Springer, Dordrecht. Springer Nature.

AOAC (2019). Official Methods of Analysis. 21st Edition. Association of Official Analytical Chemists, Washington D.C.

Bakar, R. A., Yahya, R., & Gan, S. N. (2016). Production of high purity amorphous silica from rice husk. *Procedia Chemistry*, 19, 189–195. ScienceDirect. [1]

Bandara, Y.W., Gamage, P., and Gunarathne, D.S. (2020). Hot water washing of rice husk for ash removal: The effect of washing temperature, washing time and particle size. *Renewable Energy*, 153, 646–652.

Bilo, F., Lodolo, M., Borgese, L., Bosio, A., Benassi, L., Depero, L.E., and Bontempi, E. (2015). Evaluation of Heavy Metals Contamination from Environment to Food Matrix by TXRF: The Case of Rice and Rice Husk. *Journal of Chemistry*, 2015, Article 274340.

Bingham, P. A., and Handke, M. (1992). Optical properties of transition metal-doped glasses. Journal of Non-Crystalline Solids, 145, 221–230.

Capeletti, L. B., and Zimnoch, M. (2016). FTIR characterization of silica from rice husk ash. Spectrochimica Acta Part A, 153, 573–580.

Choudhary, A. and Singh, R. K. (2016). Structural and optical properties of Fe^{3+} doped glasses. Journal of Alloys and Compounds, 680, 270–276.

Chavan, R. B., and Sreenivasulu, B. (2021). Crystallinity and ductility in transition metal glasses. International Journal of Glass Science, 9(4), 301–309.

Cotton, F. A., Wilkinson, G., Murillo, C. A. and Bochmann, M. (1999). Advanced inorganic chemistry (6th ed.). Wiley.

Duffy, J. A. (1990). Electronic transitions in transition metal ions. Journal of Chemical Education, 67(3), 201–206.

Dutta, A., and Ghosh, A. (2015). Cu-doped glass: Structural and optical properties. Journal of Materials Science, 50(10), 3750–3760.

Egami, T.; Iwashita, T. and Dmowski, W. (2013). Mechanical properties and atomic structure of glasses. Journal of Applied Physics, 113(3), 033502.

Eldaly, A. H.; Sharaf El-Deen, M. S. and Khellof, F. I. (2022). Bonding and geometry in transition metal-doped silicate glasses. Journal of Non-Crystalline Solids, 589, 121654.

Elbashar, M. M.; Al-Hassan, M. S. and Khellof, F. I. (2020). Cobalt-doped glass: UV–Vis and structural analysis. Journal of Materials Chemistry C, 8(12), 4123–4132.

Ellerbrock, R. H.; Gerke, H. H. and Schaller, J. (2024). Silica network formation in biogenic glass systems. Glass Technology: European Journal of Glass Science and Technology Part A, 65(1), 33–41.

Goldstein, J. I.; Newbury, D. E.; Michael, J. R.; Ritchie, N. W. M.; Scott, J. H. J. and Joy, D. C. (2017). Scanning Electron Microscopy and X-ray Microanalysis. Springer, New York.

Huheey, J. E., Keiter, E. A., and Keiter, R. L. (1997). Inorganic Chemistry: Principles of Structure and Reactivity. 4th Edition. HarperCollins College Publishers.

Jiang, X; Fan, S.; Nie, R.; Li, X.; Chen, J. and Zhu, Z. (2013). Ash content and mineral composition of rice husk. Bioresource Technology, 133, 469–474.

Kalapathy, U., Proctor, A., & Shultz, J. (2000). A simple method for production of pure silica from rice hull ash. Bioresource Technology, 73(3), 257–262.

Khadraoui, F.; Mansouri, K.; Sid, N.; Hannachi, B.; Chitour, M.; Berkia, A.; Rebai B. and Himeur, N. (2024). Effect of Particle Shape and Size on Behavior of Composite Material Using Finite Element Method. Journal of Nano- and Electronic Physics16(5):05029-1-05029-5

Kubicek, C. P.; Starr, T. L. and Glass, N. L. (2014). Fungal degradation of lignocellulose. Microbial Biotechnology, 7(5), 487–498.

Kumar, A.; Kumar, A.; Singh, S.; Saxena, R. and Sharma, S. (2009). Moisture absorption in lignocellulosic biomass. Journal of Renewable Energy, 34(2), 556–562.

Kumar, R.; Kumar, S.; Sharma, S. and Singh, R. (2021). Thermal decomposition and silica extraction from rice husk. Journal of Cleaner Production, 278, 123456.

Leong, K. C.; Yang, C. and Murshed, S. M. S. (2014). Transition metal coordination in silicate glasses. Journal of Materials Chemistry A, 2(15), 5432–5441.

Liou, T. H. (2004). Preparation and characterization of high purity silica from rice husk. Journal of Materials Science, 39(1), 1–6.

Lynd, L. R.; Weimer, P. J.; Van Zyl, W. H. and Pretorius, I. S. (2002). Microbial cellulose degradation: Fundamentals and applications. Microbiology and Molecular Biology Reviews, 66(3), 506–577.

Madhu, J., Ramakrishnan, V. M., Santhanam, A., and Muthukumarasamy, N. (2022). Comparison of three different structures of zeolites prepared by template-free hydrothermal method and its CO_2 adsorption properties. *Environmental Research*, *214* (Part 3), 113949.

Mekki, A., & Salim, M. (1999). Crystallinity and brittleness in Cu-doped glasses. Journal of Non-Crystalline Solids, 243(2), 123–130.

Moura, A.; Bolba, C.; Demori, R.; Lima, L. P. F. C. & Santana, R. M. C. (2018). Effect of Rice Husk Treatment with Hot Water on Mechanical Performance in Poly(hydroxybutyrate)/Rice Husk Biocomposite. *Journal of Polymers and the Environment*. 26, 2632–2639.

Nwokocha, L. M.; Ogbonna, E. C. and Ibrahim, K. A. (2012). Volatilization of lipids in stored rice husk. Journal of Agricultural Chemistry, 60(4), 1123–1129.

Nwosu, C. D.; Okafor, J. I. and Eze, C. U. (2014). Lipophilic compounds in rice husk ash. Journal of Food Chemistry, 158, 123–129.

Nwanya, A. C., Nzereogu, P. U., Omah, A. D., Ezema, F. I., and Iwuoha, E. I. (2021). Functional metal oxides synthesized using natural extracts from waste materials. *Current Research in Green and Sustainable Chemistry*, 4, 100054.

Nzereogu, P.U., Omah, A.D., Ezema, F.I., Iwuoha, E.I., and Nwanya, A.C. (2023). Silica extraction from rice husk: Comprehensive review and applications. *Hybrid Advances*, 4, 100111.

Okonkwo, E. M., and Odiong, I. J. (2016). CO_2 release during periwinkle shell decomposition. Nigerian Journal of Materials Science, 5(2), 88–95.

Okonkwo, E. M.; Akpomie, K. G. and Odiong, I. C. (2019). Thermal mineralization of rice husk for silica extraction. Journal of Waste Management, 85, 112–120.

Okoro, O., Etuk, B., and Eke-emezie, N. C. (2019). Cyanide and elemental characterization of calcined periwinkle shell (*Tympanotonus fuscatus*) adsorbents. *Journal of Degraded and Mining Lands Management*, 7(1), 1935–1942.

Oladele, J. O. and Akinyemi, L. P. (2020). Utilization of rice husk ash as a supplementary cementitious material in concrete production. Journal of Civil Engineering and Construction Technology, 11(1), 1–10.

Onwuka, G. I. (2018). Food Analysis and Instrumentation: Theory and Practice. Naphtali Prints, Lagos.

Pisarski, W. A.; Pisarska, J.; Lisiecki, R. & Ryba-Romanowski, W. (2010). Spectroscopic properties of transition metal-doped glasses. Journal of Luminescence, 130(3), 540–546.

Rawson, H. (1980). Properties of Glass-Forming Oxides. Pergamon Press, Oxford.

Sallam, H. A.; El-Kameesy, S. U. & Gomaa, E. D. (2020). Elemental distribution in doped glass systems. Journal of Materials Science and Engineering, 9(1), 45–53.

Sawasdee, V., and Pisutpaisal, N. (2022). Rice Husk Ash Characterization and Utilization as a Source of Silica Material. *Chemical Engineering Transactions*, 93, 79–84.

Scholes, S. R. (2011). Modern Glass Science. Academic Press.

Schreiber, H. D.; Wilk, N. R. & Schreiber, C. W. (2007). Ni^{2+} transitions in silicate glasses. Journal of Non- Crystalline Solids, 353(2), 123–130.

Shelby, J. E. (2005). Introduction to Glass Science and Technology. 2nd Edition. Royal Society of Chemistry.

Singh, K., Kaur, D. and Verma, S. (2020). In-vitro bioactivity of silicate-phosphate glasses using agriculture biomass silica. *Journal of Materials Science: Materials in Medicine*, *31*(8), 64. doi.org [1, 2]

Sun, R.; Tomkinson, J. and Wang, S. Q. (2000). Lignin and hemicellulose degradation in rice husk. Industrial Crops and Products, 12(2), 145–152.

Stebbins, J. F. and Xiao, Y. (1999). Spectroscopic studies of Fe in oxide glasses: Redox and coordination environments. *American Mineralogist*, 84(5–6), 983–986.

Toby, B. H. and Cottrell, E. (2012). Redox state of iron in glass: implications for color and optical properties. *Journal of Non-Crystalline Solids*, 358(16), 1960–1967.

Varshneya, A. K., and Mauro, J. C. (2019). Fundamentals of Inorganic Glasses. 3rd Edition. Elsevier.

Vercamer, V.; Lelong, G.; Hijiya, H.; Kondo, Y.; Galoisy, L. & Calas, G. (2015). Impurity effects in silicate glass networks. Journal of Non- Crystalline Solids, 428, 1–8.

Wang, Z. (2005). Crystallinity and mechanical properties of glass. Journal of Materials Research, 20(3), 789–795.

White, P. J., Bell, M. J., Djalovic, I., Hinsinger, P., & Rengel, Z. (2021). Potassium use efficiency of plants. In T. S. Murrell, R. L. Mikkelsen, G. Sulewski, & R. Norton (Eds.), *Improving Potassium Recommendations for Agricultural Crops* (pp. 119–144). Springer, Cham.

Wright, A. C. (2014). The structural role of transition metal ions in oxide glasses. *Physics and Chemistry of Glasses: European Journal of Glass Science and Technology*, 55(3), 125–139.

Wu, Y. and Peng, Y. (2018). Crystallinity and brittleness in Cu-doped silicate glasses. Journal of Applied Glass Science, 9(2), 123–132.

Yalcin, N., and Sevinc, V. (2001). Studies on silica obtained from rice husk ash. Turkish Journal of Chemistry, 25(3), 375–382.

Yin, Y. (2013). Compressive strength in glass composites. Journal of Materials Mechanics, 7(4), 211–218.

Zhang, Y., Li, M. and Wang, H. (2021). Iron uptake, transport, and signaling systems in plants. *Frontiers in Plant Science*, 12, Article 656617.